Penta nitrogen coordinated cobalt single atom catalysts with oxygenated carbon black for electrochemical H$_2$O$_2$ production

Wenjun Zhang [a,b,1], Jae Won Choi [a,1], Sooyeon Kim [c,1], Thao Thi Le [b,d], Subhajit Nandy [e], Chang-Kyu Hwang [a,f], Sae Yane Paek [a,g], Ayeong Byeon [h], Keun Hwa Chae [e], Seung Yong Lee [a,b], Sang Hoon Kim [b,d], Hakhyeon Song [i], Jaehoon Kim [i], Jihun Oh [i], Jae W. Lee [h], Sang Soo Han [c,*], Jong Min Kim [a,b,j,**]

[a] Materials Architecturing Research Center, Korea Institute of Science and Technology, 5 Hwarang-ro 14-gil, Seongbuk-gu, Seoul 02792, Republic of Korea
[b] Division of Nano & Information Technology, University of Science and Technology, 217 Gajeong-ro, Yuseong-gu, Daejeon 34113, Republic of Korea
[c] Computational Science Research Center, Korea Institute of Science and Technology, 5 Hwarang-ro 14-gil, Seongbuk-gu, Seoul 02792, Republic of Korea
[d] Extreme Materials Research Center, Korea Institute of Science and Technology, 5 Hwarang-ro 14-gil, Seongbuk-gu, Seoul 02792, Republic of Korea
[e] Advanced Analysis Center, Korea Institute of Science and Technology, 5 Hwarang-ro 14-gil, Seongbuk-gu, Seoul 02792, Republic of Korea
[f] Department of Micro/Nano System, Korea University, 145 Anam-ro, Seongbuk-gu, Seoul 02841, Republic of Korea
[g] Department of Energy Engineering, Hanyang University, 222 Wangsimni-ro, Seongdong-gu, Seoul 04763, Republic of Korea
[h] Department of Chemical and Biomolecular Engineering, Korea Advanced Institute of Science and Technology, 291 Daehak-ro, Yuseong-gu, Daejeon 34141, Republic of Korea
[i] Department of Materials Science and Engineering, Korea Advanced Institute of Science and Technology, 291 Daehak-ro, Yuseong-gu, Daejeon 34141, Republic of Korea
[j] KHU-KIST Department of Converging Science and Technology, Kyung Hee University, Seoul 02447, Republic of Korea

A R T I C L E   I N F O

A B S T R A C T

The two-electrons (2e$^-$) oxygen reduction reaction (ORR) offers a sustainable and decentralized alternative to the traditional synthetics for hydrogen peroxide (H$_2$O$_2$) production. Although various Co single atom catalysts (SACs) have been proposed as highly effective 2e$^-$ ORR catalysts, there is still room for improvement through fine-tuned coordination environment. Here, a Co-N$_5$-O-C with the combination of highly coordinated Co-N$_5$ moieties and nearby electro-withdrawing epoxides is first time developed to reach the optimal binding energy of *OOH intermediate, resulting in the ultrahigh mass activity of 87.5 A g^{-1} at 0.75 V vs. RHE. Moreover, a high H$_2$O$_2$ production rate of 11.3 mol g^{-1} h^{-1} at 200 mA cm^{-2} is also obtained by a flow cell device. Such an efficient in-situ generation of H$_2$O$_2$ further enables 100% degradation of the organic methylene blue pollutant within 15 min through the electro-Fenton process. These findings will provide a new direction for on-site H$_2$O$_2$ synthesis and wastewater treatment.

1. Introduction

As an eco-friendly oxidant, hydrogen peroxide (H$_2$O$_2$) is commonly used in numerous fields as sterilizing and bleaching agents and reaction reagents evident by its considerable production scale and fast-growing market [1–3]. Currently, H$_2$O$_2$ production relies on complex anthraquinone processes via sequential hydrogenation and oxidation reactions [4]. However, this method is an energy-intensive,

reprocessing-complicated, and environmentally threatening route. In addition, the instability of high-concentration H$_2$O$_2$ products also poses a safety risk to the shipment and storage process. As an alternative, a decentralized strategy (i.e., direct synthesis) has been developed to produce H$_2$O$_2$ through the direct reaction of H$_2$ and O$_2$ gases; however, this procedure is particularly explosive and requires the use of expensive noble metal catalysts [5,6]. Based on the drawbacks of the two methods mentioned above, a greener and safer electrochemical method for H$_2$O$_2$

production via the two-electrons oxygen reduction reaction (2e$^-$ ORR) route has gained much attention in recent decades [7,8]. Moreover, by coupling this method with accessible and environmentally friendly power sources such as wind or solar, a cost-effective water purification device can be developed by implementing flow cells with optimized configurations in an aqueous environment, in which a continuous and scalable H_2O_2 production can be achieved in the presence of a highly efficient electrochemical catalyst [9,10]. However, in practical applications, these H_2O_2 electroreactors usually exhibit low efficiency and poor stability mainly due to the lack of highly active, selective, and durable electrocatalysts in high overpotential windows [11]. Thus, the optimized structure of catalysts should be designed to reasonably boost the activity of the 2e$^-$ ORR process.

Among the promising candidates for 2e$^-$ ORR catalyst, single atom catalysts (SACs) have been attracting much interest due to their unique and tunable electronic structure and maximum atom-utilization efficiency because SACs induce end-on chemisorption of O_2, improving the selectivity for the 2e$^-$ ORR rather than the 4e$^-$ ORR [12,13]. The catalytic activity of the 2e$^-$ ORR for H_2O_2 production is determined by the binding energy of the intermediate *OOH (* denotes a surface site). Cost-effective and environmentally benign transition metal catalysts such as Fe, Ni, and Co have been studied for 2e$^-$ ORR catalysts, and it has been proven experimentally and theoretically that Co has the most suitable binding energy of *OOH for H_2O_2 generation [14–16]. Although the Co-N$_4$ moiety, which is found in a metalloenzyme that exists in nature, is regarded as the most stable and representative form of Co SAC, it is also kinetically favorable for the 4e$^-$ ORR pathway, generating H_2O as a final product [17]. Thus, to further improve the selectivity and activity towards H_2O_2 generation, a strategy by tailoring the coordination environment around the Co SAC is required. It is suggested that the catalytic properties of SAC can be optimized by controlling the coordination environment between the metal center and ligand in the first coordination sphere and introducing functional groups in the second coordination sphere [18–21]. Controlling nearby N number of coordinated center Co or replacing the partial substitute of N into O in the first coordination sphere to form Co-N$_x$O$_y$ SACs can alter charge redistribution and modulate the d-band centers of the metal atoms, resulting in the optimal electronic structure of the active sites and shift of the reaction pathway from 4e$^-$ ORR to 2e$^-$ ORR [22]. For example, Co-N$_2$, Co-N$_2$O$_2$, and Co-N$_5$ have been explored to control the coordination structure of Co, and they exhibit a more superior 2e$^-$ ORR activity than that of Co-N$_4$ [18,23,24]. In particular, Metal-N$_5$ (five-coordinated structure) exhibits superior electrocatalytic properties than that of symmetric M-N$_4$ due to its asymmetric electronic structure, which has been demonstrated in various electrochemical applications such as CO$_2$RR, Li-S batteries, and Zn-Air batteries [25–27]. Moreover, due to the positive effect of O functional groups like oxidized carbon based material on the activation of 2e$^-$ ORR, it is highly believed that in insertion of the highly active O species like epoxy O in the second coordination sphere of the carbon matrix to incorporate with Co-N$_x$O$_y$ can also promote the 2e$^-$ ORR by modulating the electronic structure of Co SACs [28–32]. Therefore, it is very important to simultaneously design and control the coordination environments between Co SACs and ligands (i.e., first coordination sphere) together with the introduction of oxygen functional groups in the second coordination sphere to unlock the full potential of Co SACs for highly effective H_2O_2 production.

Here, we propose a highly coordinated and epoxy-rich Co-N$_5$-O-C catalyst designed with one of the most optimal atomic structures among the Co SACs reported to date for high-performance electrochemical H_2O_2 production by 2e$^-$ ORR. Through a simple modified ligand-mediated method, the epoxy-rich Co-N$_5$-O-C catalyst was successfully synthesized. The synergistic effect between the Co-N$_5$ centers and the neighboring epoxy oxygen can significantly boost both the selectivity and activity for the 2e$^-$ ORR. In particular, the epoxy-rich Co-N$_5$-O-C structure showed excellent selectivity (85.6% at 0.75 V vs. RHE), 15% higher than that of the epoxy-deficient Co-N$_5$-C. Moreover, an ultrahigh

mass activity of 87.5 A g^{-1} was achieved at 0.75 V vs. RHE. From density functional theory (DFT) calculations, we found that the Co-N$_5$ moiety has a lower overpotential for the 2e$^-$ ORR than that of the Co-N$_4$ moiety, and the presence of epoxy groups near the Co-N$_5$ centers further decreases the overpotential, leading to the enhanced activity of H_2O_2 electrosynthesis. Furthermore, by using the synthesized Co-N$_5$-O-C catalyst as a cathode for a flow cell device, mass production of H_2O_2 was achieved with a production rate of 11.3 mol g^{-1} h^{-1} at a current density of 200 mA cm^{-2}. Moreover, a high faradaic efficiency of ~80% was maintained during 24 h of testing, showing good stability for practical use. Additionally, by taking advantage of its excellent performance for in-situ H_2O_2 electrochemical generation, the Co-N$_5$-O-C electrode combined with conductive carbon fiber paper further enabled the effective degradation of a non-biodegradable toxic organic pollutant through an optimized electro-Fenton system, showing great potential for on-site wastewater treatment applications.

2. Experimental

2.1. Chemicals

Cobalt(II) phthalocyanine (CoPc, 97%), and 1,10-phenanthroline ($\geq$99%), cerium (IV) sulfate (Ce(SO$_4$)$_2$, $\geq$ 99.9%), potassium hexacyanoferrate (III) (K$_3$Fe(CN)$_6$, $\geq$ 99.0%), potassium cyanide (KCN, $\geq$96.0%), perchloric acid (HClO$_4$, 70%), nitric acid (HNO$_3$, 70%), and Methylene blue (MB, 0.05 wt% in H_2O, Sigma Aldrich) were purchased from Sigma Aldrich. Dimethylformamide (DMF, 99.5%), potassium hydroxide (KOH, 93%), sodium sulfate anhydrous (Na$_2$SO$_4$, 99%), ethyl alcohol (anhydrous, 99.9%) were purchased from Daejung Chemical. Sulfuric acid (H$_2$SO$_4$, 98%) was purchased from Baker Analyzed™ A.C. S. Reagent. Vulcan XC-72R carbon black (C) was purchased from the fuel cell store.

2.2. Synthesis of CoPc/O-C hybrids

In a typical synthesis, 500 mg of C was added into 500 mL of 12.0 M HNO$_3$ solution. Then, the above mixture was refluxed at 85 ℃ for 3 h to obtain oxidized C (O-C) [9]. After natural cooling, the slurry was taken out, centrifuged, and washed with water and ethanol several times until the pH was neutral. Finally, the sample was dried at 70 ℃ in a vacuum oven for further use. Based on the reported ligand-mediated method, 10 mg of CoPc and 30 mg of 1,10-phenanthroline were dispersed into DMF solution followed by 30 min of sonication. Subsequently, 70 mg of obtained O-C was added to this solution, and the resulting solution was heated in a water bath at 60 ℃ for 4 h under continuous stirring. The resulting dispersion was then dried at 100 ℃ under vacuum conditions overnight to evaporate the DMF, yielding a black powder [33]. After that, it was lightly ground with a mortar and pestle, then transferred into a ceramic crucible and placed in a tube furnace for 2 h pyrolysis at 600 ℃ under an argon atmosphere at the heating rate of 10 ℃ min^{-1}. The final product was obtained after cooling to room temperature and denoted as Co-N$_5$-O-C. Likewise, the Co-N$_5$-C sample was also produced by the same method except for the change of carbon support from O-C to untreated C. The other three CoPc/O-C hybrids were also obtained using a similar procedure, except that the amount of CoPc used was increased to 30 (2.3 wt%), 50 (2.9 wt%), and 150 mg (5.9 wt%), respectively.

2.3. Materials characterization

Scanning electron microscope (SEM) was performed on FEI Inspect F50 electron microscope operated at 10 kV. High-angle annular dark-field scanning transmission electron microscopy HAADF-STEM images were obtained by using a Titan 80–300 scanning/transmission electron microscope operated at 300 kV, equipped with a probe spherical aberration corrector. Energy dispersive spectroscopy (EDS) mapping was carried out using the Talos microscope working at 200 kV equipped with

an extreme-field emission gun (X-FEG) and super-X EDS system with four silicon drift detectors (SDDs). Extended X-ray absorption fine-structure (EXAFS) measurements for Co K-edge and soft X-ray absorption near edge structure (XANES) measurements for O K-edge were done at 1D XRS KIST-PAL beamline of Pohang Accelerator Laboratory, South Korea. The Fourier transforms of EXAFS data were obtained by processing the Co K-edge result using the IFEFFIT software package. XRD patterns were obtained by Smartlab (Rigaku) diffractometer equipped with a Cu Kα radiation source ($\lambda = 1.5405$ Å) operating at 40 kV. Raman spectra were acquired on a Renishaw in via reflex spectrometer system, which was excited using a 532 nm diode laser (power 40 mW). XPS analysis was carried out on Nexsa (ThermoFisher Scientific) using a Microfocus monochromatic X-ray source (Al-Kα, 1486.6 eV). Fourier transform infrared spectroscopy (FT-IR) spectra were collected using Thermo fisher 10 ATR were collected over 4000–750 cm^{-1} by KBr (number of scans, 64; resolution, 4). Co content in all the samples was determined by an inductively coupled plasma optical emission spectrometry (ICP-OES, USA). UV–visible (UV-Vis) spectra were obtained on a Varian Cary 300 Bio UV-Vis spectrophotometer at 319 nm.

2.4. Electrochemical measurements

The electrochemical measurements were conducted in a three-electrode cell equipped with a rotating ring disk electrode setup (RRDE, Metrohm Autolab USA) and Autolab potentiostat (PGSTAT302N). An RRDE electrode with a glassy carbon electrode (0.196 cm^2 area) and a platinum ring electrode (0.072 cm^2 area) was used as the working electrode. Ag/AgCl electrode and platinum (Pt) wire were used as the reference electrode and counter electrode, respectively. For preparing the working electrode, the catalyst ink was prepared by dispersing 3 mg of catalyst into 1.8 mL ethanol and 50 μL Nafion (5 wt%) solution by sonication for 30 min. And then 1.24 μL of catalyst ink was drop-casted onto the disk electrode of RRDE, resulting in a catalyst loading of 10 μg cm^{-2}. All the potentials were calibrated into the potential of the reversible hydrogen electrode (RHE). The RHE calibration of the Ag/AgCl electrode was conducted in high-purity hydrogen-saturated electrolytes. The Pt wire was used as the working and counter electrode, and the Ag/AgCl reference electrode was used as the reference electrode. The electrolyte (0.1 M KOH) was first saturated with high-purity (99.999%) H$_2$ gas for at least 30 min. After that, the measurement of open circuit potential (OCP) was conducted for 10 min to obtain the saturated potential (-0.963 V vs. Ag/AgCl). It should be noted that in all subsequent experiments, the RHE calibration was performed in the same manner. Electrochemical ORR measurements were conducted in an O$_2$-saturated 0.1 M KOH electrolyte (pH~13) at room temperature. Before the ORR measurement, pre-cycling cyclic voltammetry (CV) steps with 10 cyclic sweeps from 0.05 to 1.0 V at a scan rate of 100 mV s^{-1} were applied on the disk electrode and followed by another CV measurement between 0.1 and 1 V versus RHE on ring electrode at a scan speed of 50 mV s^{-1} for 20 cycles, which helps to reach a stable cyclic voltammetry shape. After that, Linear sweep voltammetry (LSV) polarization measurements were performed under a scan rate of 10 mV s^{-1} with a rotation speed of 1600 rpm without iR correction in the used electrolytes with the fixed potential of the platinum ring electrode at a constant potential of 1.20 V vs RHE, which was recorded at the range of 0.05–1 V. The same procedures were also done in 0.1 M Na$_2$SO$_4$ (pH~6.8) and 0.1 M HClO$_4$ (pH~1) electrolytes respectively at 298 K. The H$_2$O$_2$ selectivity (%) and electron transfer number (n) were obtained from LSV polarization curves of the corrected disk current (I$_d$) and ring current (I$_r$) between the data obtained in Ar-saturated electrolyte and the O$_2$-saturated electrolyte from the following Eq. (1) and Eq. (2):

$$Selectivity\ (100\%) = 200 \times (I_r/N)/(I_d + I_r/N) \tag{1}$$

$$Electrons\ transferred\ number\ (n) = 4 \times I_d/(I_d + I_r/N) \tag{2}$$

Here, the collection efficiency (N) of RRDE was determined to be

0.250 using a typical redox system of K$_3$Fe(CN)$_6$ solution, which calculation came from Eq. (3):

$$N = I_r/|I_d| \tag{3}$$

The kinetic current density (J$_k$) was then extracted by correcting the mass transport losses, according to Koutecký–Levich method (Eq. (4)):

$$I/J_m = 1/J_l + 1/J_k \tag{4}$$

where J$_m$ indicates the measured total current density and J$_l$ is the diffusion-limited current density. Usually, it is difficult to determine the value of the limiting current, usually determined from the highest steady current measured in the entire potential range, in most of the carbonaceous catalysts. Thus, we calculated the limiting current from the Levich equation by using the obtained electron transfer number (n) in RRDE results through Eq. (5):

$$Il = 0.62nFAD_0^{2/3}\omega^{1/2}\nu^{-1/6}DC_0 \tag{5}$$

Where F, A, D$_0$, ω, υ and C$_0$ indicate the Faraday constant (96,485 C mol^{-1}), geometric area of the disk electrode (0.196 cm^2), the diffusion coefficient of O$_2$ in the electrolyte at 298 K (1.85 × 10^{-5} cm^2 s^{-1}), electrode rotation speed (rad s^{-1}), the kinematic viscosity of O$_2$ (0.89 × 10^{-2} cm^2 s^{-1}) and O$_2$ concentration (1.21 × 10^{-6} mol cm^{-3}). The mass activity was calculated at 0.65 V and at 0.75 V by dividing the kinetic current by the mass loading of ink, here we use the commercial carboxylic acid functionalized as a reference sample.

2.5. Flow cell test

H$_2$O$_2$ production rate, faradaic efficiency (FE, %), and stability test of the electrocatalysts for H$_2$O$_2$ production were evaluated using a three-electrode flow-cell electrolytic device. A catalyst ink was prepared by dispersing 4 mg of catalyst into 2 mL ethanol and 67 μL Nafion (5 wt%) solution. The following ultrasonication for 1 h to form a uniform dispersion, all the ink was coated on commercial carbon paper (Sigracet 39 BB, SGL Carbon Group) by spray gun and dried under 80 ℃ (the catalyst loading was 0.8 mg cm^{-2}). The catalyst-modified carbon paper was subsequently used as the working electrode in the three-phase flow cell device, with Hg/HgO as the reference electrode and commercial NiFeMo alloys as the counter electrode with a high OER activity in alkaline conditions. The electrolyte for both cathode and anode was 1 M KOH (40 mL). The electrolyte was circulated through the electrochemical cell using a peristaltic pump (flow rate 40 mL min^{-1}). Simultaneously, a continuous flow of O$_2$ was introduced into the cell (20 mL min^{-1}). Constant currents from 20 to 600 mA were applied to the working electrode for H$_2$O$_2$ evolution. Electrolyte samples in the cathode part were taken in each test after 30 min, and then titrated against Ce^{4+} to evaluate the H$_2$O$_2$ production rate (e.g. 2Ce^{4+} + H$_2$O$_2$ → 2Ce^{3+} + 2 H$^+$ + O$_2$) since the amount of H$_2$O$_2$ evolved can be calculated as twice the molar amount of Ce^{4+} consumed [34]. In more detail, first, Ce(SO$_4$)$_2$ was dissolved in 0.5 M H$_2$SO$_4$ to prepare a series of standard Ce^{4+} solutions (up to 0.6 mM). Absorption spectroscopy of standard Ce^{4+} solutions was then performed on UV–vis from 800 to 300 nm, and a calibration curve at 319 nm was generated according to the following Eq. (6):

$$Abs = \varepsilon \times l \times \left[Ce^{4+}\right] \tag{6}$$

where Abs is the absorbance at 319 nm, [Ce^{4+}] is the Ce^{4+} concentration (mM), ε is the molar absorptivity of Ce^{4+} (mM^{-1} cm^{-1}), and l is the path length.

Thus, to indirectly check the H$_2$O$_2$ production rate by Eq. (7), consumed Ce^{4+} was determined by the concentration difference which can be measured by the solution absorbance at 319 nm of Ce(SO$_4$)$_2$ as a stock solution (0.6 mM, determined from calibration curve) in 0.5 M H$_2$SO$_4$ before and after injecting aliquot of electrolyte taken out of

the working electrode in cathode compartment at specific time intervals during electrolysis.

$$H_2O_2 \ concentration = \frac{[Ce^{4+}]_{Before} - [Ce^{4+}]_{after}}{2 \times V_{titration}} \times 40 \qquad (7)$$

$V_{titration}$ means the volume of the electrolyte taken from 40 mL of KOH electrolyte for titration. Faradaic efficiency can be described by the following Eq. (8):

$$Faradaic \ efficiency(\%) = \frac{100 \times 2 \times 96485 \times H_2O_2 \ production \ yield}{\int_0^t Idt} \qquad (8)$$

where $\int_0^t Idt$ stands for the cumulative charge passed (C) during electrolysis.

When evaluating the stability of the electrocatalysts and H_2O_2 production, 500 mL electrolyte (1 M KOH) was circulated through the electrochemical cell using the same flow rate of the pump (40 mL min^{-1}) and also the same O_2 flow rate (20 mL min^{-1}). Here constant current testing at 200 mA was carried out for 24 h to evaluate catalyst stability for H_2O_2 production, with H_2O_2 in the electrolyte being quantified using a similar abovementioned Ce^{4+} titration method.

2.6. DFT Computational details

Spin-polarized Density functional theory (DFT) calculations were performed using the Vienna Ab initio Simulation Package (VASP) software package [35,36]. Projector-augmented wave (PAW) potentials were used to describe core-valence electron interactions and the generalized gradient approximation (GGA) of the Perdew-Burke-Ernzerhof (PBE) exchange-correlation functional was used [37,38]. The plane-wave cutoff energy was set to 550 eV. All atoms were fully relaxed to force tolerance of 0.01 eV/Å, and a convergence criterion of 10^{-6} eV was employed for the electronic self-consistent iteration. Gaussian smearing was used to determine the electronic occupancies with a smearing width of 0.10 eV. The *k*-point was set to $4 \times 4 \times 1$ using the gamma-centered grid. Dipole corrections along the z-axis were included in all calculations, and the DFT-D3 method of Grimme was used for van der Waals (vdW) corrections [39]. Solvation effects were considered using the continuum solvation model ($\varepsilon = 78.5$) implemented in VASPsol [40].

To model the Co-N$_5$-C and Co-N$_5$-O-C SACs, we used bilayer graphene structures, in which a 4×4 supercell was considered with a 20 Å vacuum layer in between the slabs (along the z-axis) in the periodic boundary conditions. We first constructed the Co-N$_4$ moiety on the top graphene layer and then various N coordination on the bottom layer were determined by calculating the binding energy of the Co SAC. And the distribution and location of the epoxy oxygen on the Co-N$_5$-C catalyst were investigated by examining the formation energy of epoxy oxygen near the Co-N$_5$ moiety.

The energetics of the ORR process were calculated based on the computational hydrogen electrode (CHE) model.[41] This model considers the chemical potential of ($H^+ + e^-$) to be equal to that of the gas-phase ½ H_2. The change of Gibbs free energy in each step was calculated using the following Eq. (9):

$$\Delta G = \Delta E + \Delta ZPE - T\Delta S + \Delta G_U + \Delta G_{pH} \qquad (9)$$

where ΔE is DFT calculated reaction energy, ΔZPE is the zero-point energy, TΔS is the entropic correction, ΔG_U represents the effect of applied bias ($-neU$), and ΔG_{pH} is the correction term for H^+ ion contribution at different pH conditions ($-k_BT$ pH ln10). ΔE, ΔZPE, and TΔS values for reference gas molecules (H_2, O_2, H_2O_2, and H_2O) are taken from a previous study by Tang et al [18]. The geometries of adsorbed intermediates (*O_2, *OOH, *O, and *OH) were fully optimized and the most stable configuration for each species are reported here. To

reveal the reaction selectivity between the two electrons (2e$^-$) pathway and the four electrons (4e$^-$) pathway in the ORR process, reaction energy barriers were calculated using the Climbing-Image Nudged Elastic Band (CI-NEB) method [42].

2.7. Electro-Fenton degradation

Electron-Fenton degradation tests were conducted in an undivided cell using a commercial graphite plate (12 cm^2) as the anode and Co-N$_5$-O-C/CFP which was made by spraying coating catalyst on 2.5*cm* × 5.0*cm* PTFE treated carbon fiber paper (Toray Carbon Paper TGP-H-060, 5 wt% PTFE) as the working cathode. The loading amount of the catalyst varies from 0.2, 0.4, and 0.8 mg cm^{-2}. MB with different concentrations varying from 10 to 30 mg L^{-1} was chosen as the target organic pollutant. O_2-Saturated acidified 0.05 M Na_2SO_4 (pH~3) under vigorous stirring (400 rpm) was used as the electrolyte solution, which was operated under different constant potentials (1, 2, and 3 V corresponding to the current density of ~7.5, 6.0, and 3.75 mA cm^{-2}, respectively) by using a direct DC power supply (LW longwei, LW K3010D) [43,44]. Fe^{2+} with different concentrations (025, 0.05, and 0.2 mM) were added to the electrolyte solution as the Fenton catalyst, respectively. A small aliquot of electrolyte solution (0.6 mL) was periodically measured at 664 nm by UV–vis spectrophotometry to determine the organic dye concentration (Shimadzu UV-2600i). Here, the efficiency of MB removal was calculated (Eq. (10)) and the corresponding kinetic first-order rate constant of MB degradation was obtained by the pseudo-first-order kinetic model (Eq. (11)) as follows:

$$MB \ removal \ efficiency(\%) = 1 - \frac{[MB]_t}{[MB]_0} \qquad (10)$$

$$Ln\left(\frac{[MB]_t}{[MB]_0}\right) = -kt \qquad (11)$$

where $[MB]_0$ (mg L^{-1}) is the initial concentration of MB solution, $[MB]_t$ (mg L^{-1}) is the concentration of MB solution during the reaction at time t (min), and k is the first-order rate constant (min^{-1}).

3. Result and discussions

The overall synthetic scheme to prepare the Co-N$_5$-C and Co-N$_5$-O-C catalysts are shown in Fig. 1. To synthesize the catalysts, we modified and used a previously reported ligand-mediated method [45,46]. Based on the modified ligand-mediated method (see the experimental procedures for details), a high-coordinated Co-N$_5$ configuration was derived from cobalt phthalocyanine (CoPc) with four pyridinic-N atoms and 1, 10-phenanthroline as an additional N source to form the penta N coordinating the Co SAC. The precursor was adsorbed on a carbon black support (Vulcan carbon, C), producing the Co-N$_5$-C structure following the pyrolysis process in Ar gas at 600 ℃. During the pyrolysis, partial atomic rearrangements occurred, in which the coordination number of N to Co increased from 4 to 5. To induce a synergetic effect between the high N coordination configurations and oxygen functional groups on the 2e$^-$ ORR performance, an epoxy-rich Co-N$_5$-O-C catalyst was prepared by doping the same amount of Co on the nitric acid-treated oxidized carbon black (O-C) through the above-mentioned method for the synthesis of Co-N$_5$-C. The inductively coupled plasma mass spectrometry (ICP-MS) measurement reveals that the Co doping amount in Co-N$_5$-O-C is 1.4 wt%. The other CoPc/O-C hybrids have various Co contents from 5.9 wt% to 2.3 wt% with the aggregated spherical particles which are observed in scanning electron microscopy (SEM) images (Fig. S1). On the other hand, the Co-N$_5$-O-C with a Co amount of 1.4 wt% inherited the morphology of its carbon support without CoPc aggregates shown in the transmission electron microscopy (TEM) images of Fig. S2, suggesting that the Co atoms were uniformly anchored on the O-C. Moreover, the X-ray Powder Diffraction (XRD) and Raman spectrum (Fig. S3)
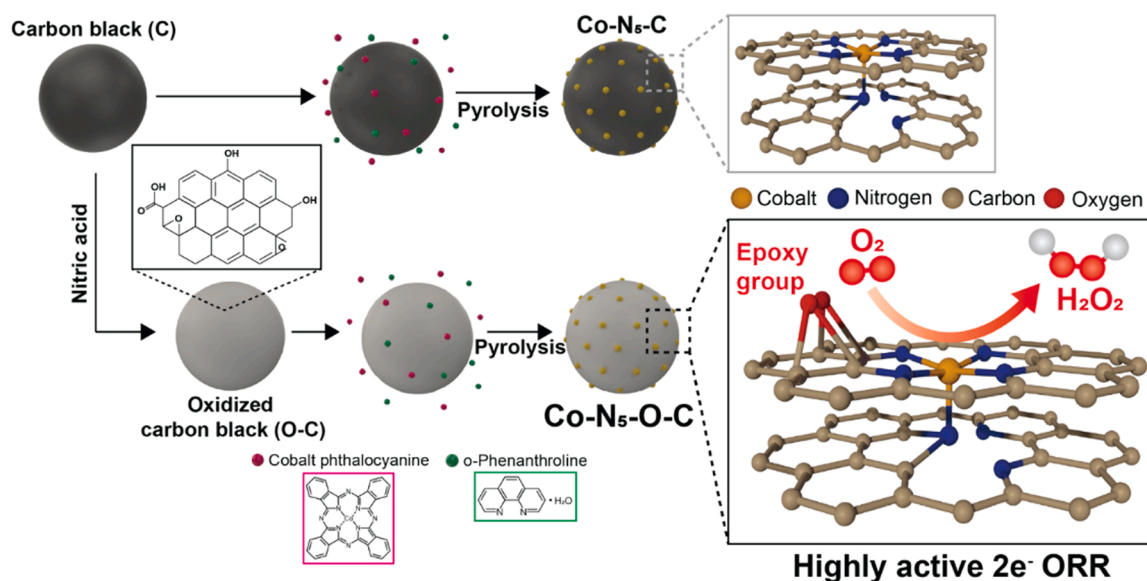
Fig. 1. Schematic illustration of the synthesis process for the Co-N$_5$ SACs.

clearly show that the peak intensity of CoPc depended on the Co content, and the peaks gradually disappeared when the doping amount decreased to 1.4 wt%, which indicates Co is likely dispersed on the O-C at a molecular level. A similar result was also obtained in the case of Co-N$_5$-C, showing a good dispersity of Co atoms (Figs. S4-S6). A high angle annular dark-field scanning transmission electron microscopy (HAADF-STEM) image was used to directly examine the dispersity of Co atoms in the as-obtained catalysts. In Fig. 2a, densely bright dots (highlighted by red circles) were clearly observed throughout the carbon matrix of Co-N$_5$-O-C, indicating the existence of the Co single atom. A similar characteristic was also observed in the Co-N$_5$-C samples (Fig. S7). The EDS elemental mapping images in Fig. 2b show the homogeneous distribution of Co, N, O, and C elements, confirming the presence of isolated Co in the samples.

To further verify the existence of SACs in the obtained Co materials and define their electronic structure and local coordination environment, synchrotron-based X-ray absorption near-edge structure (XANES) and extended X-ray absorption fine structure (EXAFS) characterizations were carried out. Here, Co foil, CoO, Co$_3$O$_4$, and CoPc were chosen as the references for comparison. As shown in Fig. S8, the near-edge absorption energy of Co-N$_5$-O-C and Co-N$_5$-C is located within the range of those of CoO and Co$_3$O$_4$ references, and Co-N$_5$-O-C shows slightly higher absorption energy than Co-N$_5$-C, implying that oxidation state of Co-N$_5$-O-C is between + 2 and + 3 and more positive than that of Co-N$_5$-C. Besides, Co K-edge Fourier transform (FT)-EXAFS in K-space and R-space are also investigated to disclose the real atomic structure of Co-N$_5$ samples (Fig. 2c and Figs. S9-S11). Obviously, in contrast with Co foil, the absence of the Co−Co scattering path (~2.19 Å) of the Co-N$_5$ catalyst gives direct evidence of the successful synthesis of Co SACs. Similar characteristic peaks to that of CoPc but different peak distribution to other references were found in the Co-N$_5$ SACs, indicating the analogical coordination environment of Co SAC with CoPc, where the Co atoms are coordinated with nitrogen to form Co–N bonds. However, both curves of the obtained Co SACs show a large distance of Co-N bond in R space than that of four N-coordinated CoPc. More precisely, from the fitted EXAFS data, the coordination number for the Co center is around 5 for both Co-N$_5$-O-C (5.0 ± 0.2) and Co-N$_5$-C (5.1 ± 0.2) samples (Table S2), which demonstrates the Co single atom is highly coordinated with five N atoms.

Elemental composition and local coordination configurations of the Co-N$_5$ moieties were investigated by X-ray photoelectron spectroscopy (XPS). The XPS survey spectra exhibit the existence of Co, N, O, and C on

the Co-N$_5$-O-C SACs (Fig. S12). The deconvoluted high-resolution N 1 s spectra (Fig. 2d) show that the pyridinic and pyrrolic N all were observed in both Co-N$_5$-O-C and Co-N$_5$-C although the pyridinic N is more dominant in both structures: Co-N$_5$-O-C (71.4%) and Co-N$_5$-C (74.6%), indicating that the pyridinic N serves as the main coordination site for the Co atoms [47]. Based on the experimental observation, we performed DFT calculations to clarify the final atomic structures of the Co SACs (Fig. S13). Here, all structures have two carbon layers, and a Co atom is coordinated with four pyridinic N atoms on the top layer; however, the bottom layer is considered with graphitic, pyridinic, and pyrrolic N atoms. Our DFT calculations indeed revealed that the Co-N$_5$ moiety can be formed only when the Co-N$_4$ moiety on the top layer binds to one of the pyrrolic N atoms on the bottom layer, i.e., the Co-N$_5$ moiety has a pyridinic N: pyrrolic N ratio of 6:1. Because it is not easy to identify whether the axial atom coordinated to the Co center is N or O from the EXAFS data, we additionally performed DFT calculations using a structure with an axial O (Co-N$_4$O$_{ax}$-C) instead of N. Our DFT calculations reveal that the Co binding in the Co-N$_4$O$_{ax}$-C is less favorable than in the Co-N$_5$-C (Fig. S14a-b). The XPS O 1 s spectra in Fig. 2e show that various oxygen functional groups such as the ketonic oxygen (C=O, 531.2 ± 0.2 eV), oxygen atoms in epoxy (C–O–C, 532.3 ± 0.2 eV), the epoxy oxygen in the ester groups (533.3 ± 0.2 eV) and oxygen atoms in carboxyl groups (534.2 ± 0.2 eV) were introduced into the Co-N$_5$-O-C as a result of the combination with the oxidized carbon matrix, which is also confirmed by the FT-IR results (Fig. S15) [31]. Noticeably, the C–O–C oxygen species was dominant in Co-N$_5$-O-C with an amount of 2.9 at%, which is around 3.6 times higher than that in Co-N$_5$-C (0.8 at %). The O 1 s spectra of carbon black (C) and oxidized carbon black (O-C) in Fig. S16 indicate that the oxidation process of carbon black induces additional epoxy groups (6.6 at% for O-C and 2.1 at% for C), revealing that the epoxy-rich configuration of Co-N$_5$-O-C originated from O-C, although the epoxy contents decrease by > 50% after the pyrolysis process.

The Co 2p XPS spectra were analyzed to determine the configuration of the epoxy oxygen and Co-N$_5$ moieties in Co-N$_5$-O-C (Fig. 2f). Co-N$_5$-O-C shows an upshift (~0.4 eV) of the peaks and a larger spin-orbit splitting of 15.596 eV compared to Co-N$_5$-C (15.505 eV), respectively. The higher binding energy and larger spin-orbit splitting indicate that the cobalt center loses electrons and is relatively more oxidized, demonstrating that the epoxy oxygen in Co-N$_5$-O-C leads to an electron-withdrawing effect in the vicinity of the Co-N$_5$ centers and the further positive charge of the Co single atom [48]. Using the pyrrolic
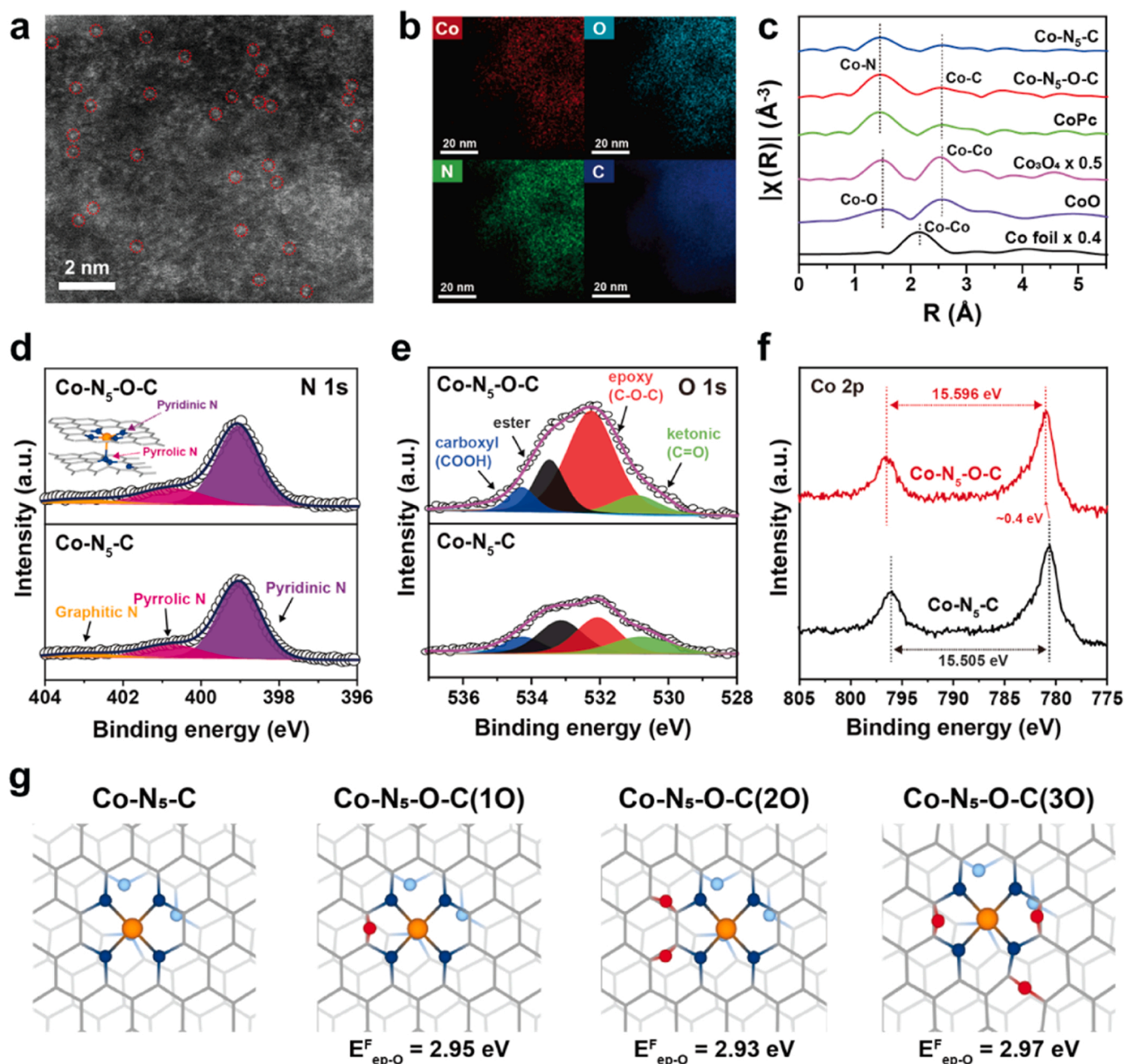
Fig. 2. Structure analyses of Co-N$_5$-O-C SACs. a) HAADF-STEM image of Co-N$_5$-O-C catalyst. b) EDS elemental mapping images for Co-N$_5$-O-C catalyst. c) Co K-edge FT-EXAFS spectra for Co-N$_5$-O-C, Co-N$_5$-C, and various reference samples. d) XPS N 1 s spectra of Co-N$_5$-O-C and Co-N$_5$-C. The inset image indicates the structure of Co-N$_5$-O-C derived from the DFT calculation. e) XPS O 1 s spectra of Co-N$_5$-O-C and Co-N$_5$-C. f) XPS Co 2p spectra of the Co-N$_5$-O-C and Co-N$_5$-C. g) The optimized geometries of the bare Co-N$_5$ moiety and Co-N$_5$ moieties with different epoxy oxygen coverages, and their calculated epoxy oxygen formation energies. Here, Co-N$_5$-C indicates the bare Co-N$_5$ moiety. Co-N$_5$-O-C (1 O), Co-N$_5$-O-C (2 O), and Co-N$_5$-O-C (3 O) indicate possible Co-N$_5$ moieties with 1, 2, or 3 epoxy oxygens in the Co-N$_5$-O-C SACs, respectively. The gray, navy, orange, and red balls represent the C, N, Co, and O atoms. Light gray and light blue are used to classify the C and N in different carbon layers.

N-coordinated Co atom model, the formation energies of the epoxy oxygen (E_{ep-O}^{F}) were calculated by DFT calculations, in which various coverages and geometries of the epoxy oxygen on Co-N$_5$ were investigated to define the plausible configuration of the Co-N$_5$-O-C SAC (Fig. S17). Here, it is noticeable that the epoxy oxygen prefers to be adsorbed on a C-C bond near N atoms, and the Co-N$_5$-C configuration with two epoxy oxygen atoms is the most favorable among the three oxygen coverages considered (1 O, 2 O, and 3 O), although the energy differences between them are marginal. The most plausible atomic structures for Co-N$_5$-C and Co-N$_5$-O-C SACs are shown in Fig. 2g. When modeling the Co-N$_5$-C structure, we did not consider the epoxy oxygen

atom(s) near the Co-N$_5$ moiety, although the small amount of epoxy oxygen is observed in Fig. 2e. According to DFT calculations, the epoxy O preferentially locates at the armchair edges of carbon substrates rather than on the basal plane at a low oxygen content, and the epoxy oxygen near the Co-N$_5$ moiety can be found mainly in Co-N$_5$-O-C rather than in Co-N$_5$-C (Fig. S18).

The ORR performance of the Co-N$_5$ SACs was evaluated to quantify the performance of the H$_2$O$_2$ production on a rotating ring-disk electrode (RRDE) at 1600 rpm in an O$_2$-saturated 0.1 M KOH electrolyte. The collection efficiency of the RRDE electrode was empirically calibrated to be 0.250 (Fig. S19). The catalyst loading amount was

optimized at 10 μg cm^{-2} to acquire the best electrochemical properties (Fig. S20 and Note S1). As shown in the ORR polarization curves (Fig. 3 a), Co-N$_5$-O-C and Co-N$_5$-C exhibited increased disk and ring current densities in the overall potential ranges compared to O-C and C, respectively. In particular, the increase in the ORR current densities of the Co-N$_5$ SACs at the high potential region is accompanied by a significant increase in the ring current densities (H$_2$O$_2$ oxidation) and H$_2$O$_2$ selectivity (Fig. 3b), indicating that the Co-N$_5$ moieties might serve as the main active sites for the generation of H$_2$O$_2$ at the high potential. To clarify the origin of the improved ORR activity of each catalyst, the active site of each catalyst was examined via a Potassium cyanide (KCN) poisoning experiment (Fig. S21), in which CN$^-$ strongly binds to single metal atom sites in its coordination structures to block intermediate adsorption on center metal sites [48]. There was no change in the ORR current densities of O-C before and after the KCN addition because carbon acts as an active site for the 2e$^-$ ORR, whereas the ORR current densities of Co-N$_5$-C and Co-N$_5$-O-C were decreased at a range of

0.4–0.9 V vs. RHE due to Co poisoning by CN$^-$ which confirmed the function of Co for working as the active sites. Apart from this, the reduction rates of the ORR current densities of Co-N$_5$-O-C and Co-N$_5$-C were 27.6% and 27.0%, at 0.65 V vs. RHE, respectively, which confirms that the contribution of the Co single atom to the ORR currents is similar for Co-N$_5$-O-C and Co-N$_5$-C. While as shown in Fig. 3, Co-N$_5$-O-C has a much higher ring current density compared to Co-N$_5$-C, Distinctively, the Co-N$_5$-O-C exhibits a higher ORR activity and higher selectivity of ~85.6% towards H$_2$O$_2$ production with the smaller electrons transferred number of around 2.3 at 0.75 V vs. RHE, which is superior to those (70.5% and 2.6 for the selectivity and electron transfer number, respectively) of the Co-N$_5$-C sample (Fig. 3b and c), implying that the epoxy groups (C-O-C) in Co-N$_5$-O-C have an important role in directing the reaction pathway toward the 2e$^-$ ORR for H$_2$O$_2$ production. A similar trend was also observed in acidic and neutral conditions (Fig. S22 and S23). In addition, the Tafel slopes were evaluated to reveal the reaction kinetics (Fig. 3d). The Co–N$_5$-O-C has the lowest Tafel slope of 40.7 mV
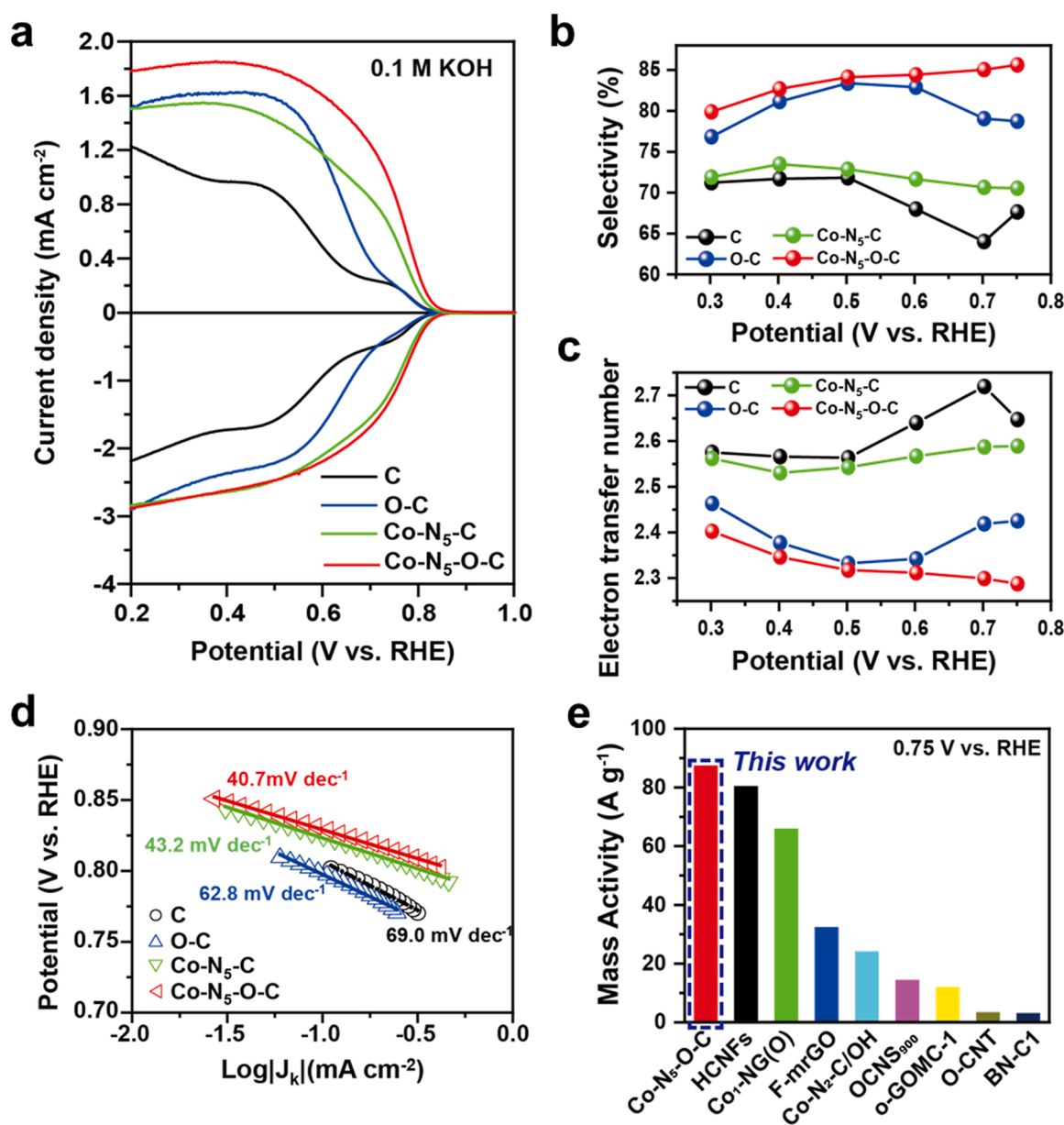

Fig. 3. ORR performance of the catalysts by RRDE. a) ORR polarization curves of the Co-N$_5$ SACs and their support carbon in 0.1 M KOH. b) Calculated H$_2$O$_2$ selectivity (%). c) the number of electrons transferred (n) for these catalysts at various potentials in 0.1 M KOH. d) Tafel plots derived from the LSV curves in a. e) Comparison of the mass activity at 0.75 V vs. RHE between Co-N$_5$-O-C and the other single atom catalysts reported in the literature under 0.1 M KOH.

dec^{-1}, outperforming those of the Co-N$_5$-C (43.2 mV dec^{-1}), O-C (62.8 mV dec^{-1}), and C (69.0 mV dec^{-1}), which demonstrates the fastest ORR kinetics of Co–N$_5$-O-C. Also, based on the Koutecky-Levich (K-L) equation, the mass-transport corrected kinetic current density for H$_2$O$_2$ production (J_k) on the Co-N$_5$-O-C catalyst was estimated as 1 mA cm^{-2} at 0.775 V vs. RHE, which is better than the various well-designed noble and none-noble electrocatalysts, revealing its superior activity for H$_2$O$_2$ synthesis (Fig. S24). In particular, it is very noticeable that Co–N$_5$-O-C SAC exhibited an ultrahigh mass activity of 87.5 A g^{-1} at a high potential of 0.75 V vs. RHE which is close to the onset potential of the HO$_2^-$/O$_2$ process and surpasses the state-of-the-art reported catalysts for the 2e$^-$ ORR as summarized in Fig. 3e and Table S3 [15]. All the above results reveal that excellent performance not only comes from the introduction of epoxy O in the second coordination layer of SAC but also the synergetic effect of the combination of the Co-N$_5$ moiety inside.

To clarify the influence of the coordination number of Co on H$_2$O$_2$ production performance, we also synthesized the four nitrogen-coordinated Co-N$_4$-O-C without an additional nitrogen source (i.e., 1,10-phenanthroline). As shown in Fig. S25, Co single atoms without any agglomeration morphologies are observed in Co-N$_4$-O-C. The amount of oxygen contained (Table S1) and configuration of oxygen functional groups in the sample is analogous to Co-N$_5$-O-C and only the oxidation state is slightly lower than Co-N$_5$-O-C (Figs. S26 and S27). Besides, the coordination number Co is determined to be 4.0 by EXAFS fitting for Co-N$_4$-O-C (Fig. S28 and Table S2). The H$_2$O$_2$ performance of Co-N$_4$-O-C was evaluated by the result comparison with previous Co-N$_5$ SACs through the RRDE test (Fig. S29). It is shown that the Co-N$_4$-O-C SAC shows the highest ORR current among all the samples, which is due to the O$_2$ being more energy favorable to absorb on Co–N$_4$ than on Co–N$_5$. However, the selectivity of Co-N$_4$-O-C is still lower than Co-N$_5$-O-C, which is probably because the reduction of *O$_2$ to *OOH on Co-N$_4$ structure requires higher overpotential and reduction of *OOH to H$_2$O$_2$ is less thermodynamically favorable than on Co-N$_5$ [24]. Besides, it is also notable that the ring current density of Co-N$_4$-O-C is higher than Co-N$_5$-C and comparable to Co-N$_5$-O-C, which is consistent with the previous result that the epoxy group steers the reaction pathway towards 2e$^-$ ORR.

Furthermore, the correlation between 2e$^-$ ORR performance and annealing temperature of CoPc/O-C mixtures during the synthesizing was investigated to find out the influence of oxygen content and Co single atom formation. Fig. S30 and S31 show SEM and TEM images of CoPc/O-C hybrids produced under 400, 800, and 1000 °C. At 400 °C, the CoPc in the mixture begins to lose mass (less than 8%) due to the minor damage to its surrounding macrocyclic structure [49] and thus the sample only exhibits traces of Co single atoms which come from the partially decomposed CoPc. In contrast, the samples annealed at 800 and 1000 °C indicate the obvious formation and growth of Co$_3$O$_4$ nanoparticles as a result of the severe collapse of the Co-N$_4$ structure in CoPc and then the subsequent reaction of free exposed Co with oxygen after removal from the oven [50], which are identified by corresponding FFT patterns (the insets of Fig. S31d and f). The Raman spectra in Fig. S32 also show the peaks at around 670 cm^{-1} of undecomposed CoPc still existing in the 400 °C sample and Co$_3$O$_4$ nanoparticles in the 800 and 1000 °C samples. The oxygen contents in these catalysts gradually decrease according to the increasing temperatures and Co-O bonding appears from 800 °C as shown in XPS O 1 s spectra (Fig. S33).

From the RRDE results, the partially decomposed CoPc at 400 °C and the nanoparticles formed at 800 °C show a significantly lower ring current than Co-N$_5$-O-C despite their high oxygen contents (Fig. S34), which manifests that the formation of Co single atom is essential for high 2e$^-$ ORR activity. Interestingly, the ORR and ring current of the 1000 °C sample are similar to those of C (Fig. 3a), and this originates from the decreased oxygen contents (2.79%) and also implies that the Co$_3$O$_4$ nanoparticles of large size (>50 nm) rarely contributes to 2e$^-$ ORR. As a result, the Co-N$_5$-O-C synthesized under 600 °C with the structure maintaining the Co-N$_4$ moieties of CoPc and fully dispersed Co atoms

shows the optimal performance for H$_2$O$_2$ production when comparing with these different thermally treated Co catalysts, which discloses the important role of the formation of Co SACs. To the best of our knowledge, among the various Co SAC reported to date, except for the fastest kinetics activity, our Co–N$_5$-O-C SAC also exhibits comparable outstanding selectivity (Table S4) under high potential (0.75 V vs. RHE) and highly positive onset potential (0.801 V, which is defined as the potential at the H$_2$O$_2$ production current density of 0.15 cm^{-2}) for H$_2$O$_2$ synthesis (Table S5), which implies that the more well designed atomic structure was found in Co SACs for the 2e$^-$ ORR.

To understand the enhanced catalytic activity of the Co-N$_5$-O-C SAC, DFT calculations were performed with the Co-N$_5$-C and Co-N$_5$-O-C SAC structures where the synergy effect of the highly coordinated Co-N$_5$ configuration and the epoxy oxygen were explored. Fig. 4a shows free energy diagrams for the 2e$^-$ ORR pathways of the Co-N$_5$-O-C SACs with several epoxy coverages at pH= 13 and 0.7 V vs. RHE, identical to our experimental conditions. Regardless of the number of epoxy oxygens up to 2, the potential determining step (PDS) is the first reduction reaction (*O$_2$ + H$_2$O + e$^-$ →*OOH + OH$^-$) rather than the second reduction reaction (*OOH + e$^-$ → HO$_2^-$). As the number of epoxy oxygens increases, not only the adsorption energies of both *O$_2$ and *OOH decrease, but the energy differences at the first reduction step also decrease. At 0.7 V vs. RHE, the second reduction of the epoxy-free Co-N$_5$ SAC is an uphill reaction; however, the introduction of the epoxy oxygen makes the reaction thermodynamically favorable where the effect is maximized with two epoxy oxygen atoms.

Although the formation of H$_2$O$_2$ becomes thermodynamically more favorable by introducing epoxy oxygen, the 4e$^-$ ORR pathway is still more downhill than the 2e$^-$ ORR pathway (Fig. S35). To understand the high faradaic efficiency property of Co-N$_5$-O-C SAC, we additionally investigated the energy barriers for the 2nd reduction reaction of the 2e$^-$ and 4 e$^-$ ORR pathways by DFT calculations with the fact that the 1st reduction reaction for the 2e$^-$ and 4e$^-$ ORR are identical and found that the 2e$^-$ ORR route is kinetically more favorable (Fig. S36).

Fig. 4b shows a volcano plot for the 2e$^-$ ORR activity of the various Co SACs on graphene supports in which ΔG*$_{OOH}$ is used as a descriptor because it has been regarded as a good descriptor for the activity of 2e$^-$ ORR catalysts [51–53]. Indeed, the Co-N$_5$ moiety exhibits a smaller overpotential than that of the Co-N$_4$ moiety, similar to Zhao et al [24]. In particular, Co-N$_5$-O-C (2 O) is closest to the volcano peak, indicating that it shows the highest activity toward H$_2$O$_2$ than that of the other catalysts tested in this study. A free energy diagram of the 2e$^-$ ORR (at 0.76 V vs. RHE) of various catalysts in Fig. 4c also shows that Co-N$_5$-O-C (2 O) has the smallest overpotential while Co-N$_5$-O-C (3 O) has the largest overpotential. The *OOH binding becomes weaker as the number of epoxy oxygens increases. Jung et al. and Zhang et al. reported weakening of the *OOH binding due to the electron-withdrawing epoxy oxygen on a Co-N$_4$ moiety [31,48]. Mun et al. investigated the effect of electron-withdrawing or -donating functionalities on the ORR activity of Fe-N-C catalysts using the change of the Fe d-orbital energy level and found that electron-withdrawing functionalities decrease the d-band energy level and weaken the binding of ORR intermediates [54]. The enhanced ORR activities of Co-N$_5$-O-C catalysts can readily be explained in the same way. We also calculated the free energy change of the Co-N$_4$O$_{ax}$-C with an epoxy O as an O$_{ax}$ for 2e$^-$ ORR pathway to investigate possibility of the O$_{ax}$ formation and its effect on the catalytic activity. Our DFT calculations reveal that the Co-N$_4$O$_{ax}$-C structure has ΔG (*OOH) of 3.62 eV. This value is even lower than that of the Co-N$_4$ moiety, indicating the lower activity than the Co-N$_4$-C (Fig. S14c). This result is not consistent to our experimental data (Fig. 3e). Therefore, we can conclude that the Co single atom is coordinated with five N atoms rather than with the O$_{ax}$ atom.

Also, the charge density changes induced by the two epoxy oxygen atoms for Co-N$_5$-O-C (2 O) are shown in Fig. 4d. Electron loss is observed in the Co atom, whereas electron accumulation is observed around the epoxy oxygen because of the electron-withdrawing effect of the epoxy
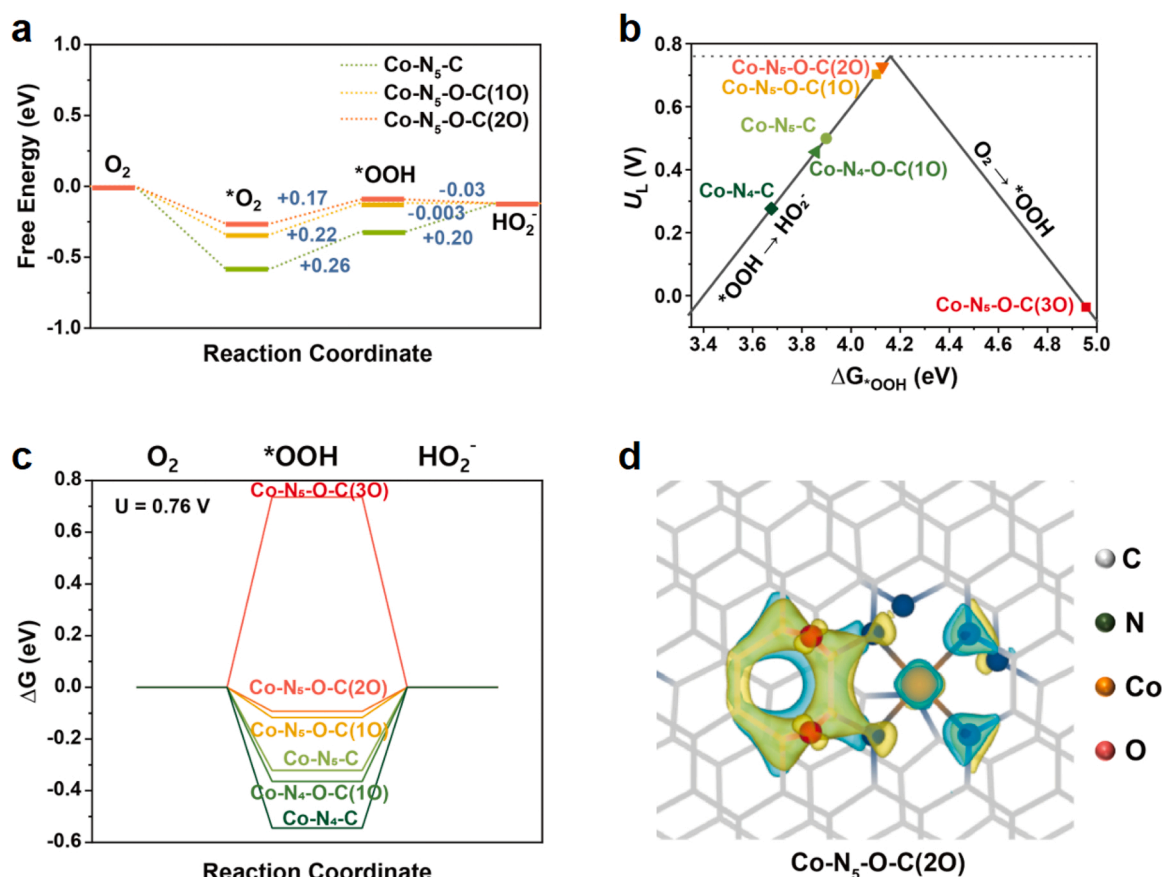
Fig. 4. DFT simulations of the electrochemical ORR performance of the catalysts. a) Free energy diagrams of the 2e⁻ ORR on Co-N₅ SACs with different epoxy coverages (Co-N₅-C, Co-N₅-O-C (1 O), and Co-N₅-O-C (2 O)) at pH= 13 and 0.7 V vs. RHE. b) The calculated volcano plot of the 2e⁻ ORR pathway to HO₂ at pH over 11.6 (The equilibrium potential of O₂/HO₂ is shown as a black dashed line). c) Free energy diagram of the 2e⁻ ORR to HO₂ at the equilibrium potential (0.76 V vs. RHE, pH > 11.6). d) Charge density differences of the Co-N₅-O-C (2 O) moiety on the graphene support. The charge density changes after introducing the two epoxy oxygen atoms are represented by yellow (electron gain) and cyan (electron loss) isosurfaces ($\pm$ 0.05 e/Bohr³) (Here, gray, navy, orange, and red represent C, N, Co, and O, respectively).

oxygen atoms. The calculated charge of Co becomes more positive by 0.05 e⁻ due to the epoxy oxygen atoms than that of the epoxy-free catalyst, which is consistent with the XPS analysis in Fig. 2f. This reveals that the electron-withdrawing effect of the epoxy oxygen readily provides an improved 2e⁻ ORR activity. Consequently, a rational design strategy for a SAC for H_2O_2 production can be applied to modulate the ΔG_{OOH*} on Co-N₅-C by providing electron-rich oxygen species near the Co-N₅ moiety.

Furthermore, by using the optimized Co-N₅-O-C SACs as the cathode catalyst of the flow cell device, mass production of H_2O_2 can be achieved on the triple-phase boundary of the gas diffusion electrode (GDE), which consists of a carbon fiber paper-made gas diffusion layer (GDL), a microporous layer (MPL), and a catalyst layer [55]. As a commonly used device for practical H_2O_2 production, the H-type cell, in which the anode chamber and the cathode chamber are separated by a polymer membrane, is based on a small amount of dissolved oxygen in the electrolyte as a reactant, so that only a low concentration of products can be obtained at a low current density [11]. In contrast, the catalyst side of a GDE in the flow cell is in contact with the electrolyte, and the other side is exposed to continuously flowing O_2 gas. This enables gas diffusion through the pores in the GDL to reach the catalyst, resulting in a facile mass transfer, a higher reaction rate, and a higher current density simultaneously schematically illustrated in Fig. 5a. The current-voltage (I-V) curves with iR compensation for different catalysts are shown in Fig. 5b. As a result, although the Co-N₅-C catalyst showed the most positive onset potential under a current density of 50 mA cm⁻², its catalytic activity was quickly exceeded by Co-N₅-O-C in the high current

range (100–200 mA cm⁻²). O- C shows a larger overpotential at the overall potential range, which is attributed to the poor ORR kinetics as shown in RRDE results. Their production rate and faradaic efficiency (FE) to H_2O_2 production in the flow cell were also recorded from 10 to 300 mA cm⁻² shown by the combined results of the Ce(SO₄)₂ titration and UV–vis spectroscopy (Fig. S37). Obviously, the Co–N₅–O-C catalyst in the flow cell showed the highest FE and the highest production rate among all the samples (Fig. 5c). Particularly, even at a high current density of 200 mA cm⁻², the FE of Co-N₅-O-C SAC reached 82.5%, much higher than those of Co-N₅-C and O-C. The production rates of representative catalysts tested by various flow cell devices within 200 mA cm⁻² are shown in Fig. 5d. Our Co-N₅-O-C catalyst exhibits a high H_2O_2 production rate of 5.92 and 11.3 mol g⁻¹ h⁻¹ at current densities of 100 and 200 mA cm⁻², respectively, higher than the reported state-of-the-art catalysts (Table S5). More importantly, it can still maintain an FE of around 80% under 24 h of testing under a high current density (100 mA cm⁻²), showing its good stability as a potential H_2O_2 catalyst for further practical applications.

In addition, to utilize the excellent H_2O_2 production performance of the Co-N₅-O-C catalyst, a user-friendly electro-Fenton process that relies on the in-situ generation of H_2O_2 to reduce the operation cost and transportation risk for wastewater treatment through advanced oxidation processes was tested [43,44,56]. In this process, the in-situ generated H_2O_2 by the cathodic 2e⁻ ORR (Eq. (12)) reacts with the added Fe^{2+} to form strong oxidizing hydroxyl radicals (·OH) (Eq. (13)), which can degrade organic pollutants into CO_2 and H_2O (Eq. (14)). Furthermore, the Fe^{2+} can be regenerated by the reduction of Fe^{3+} (Eq. (15)) [57].
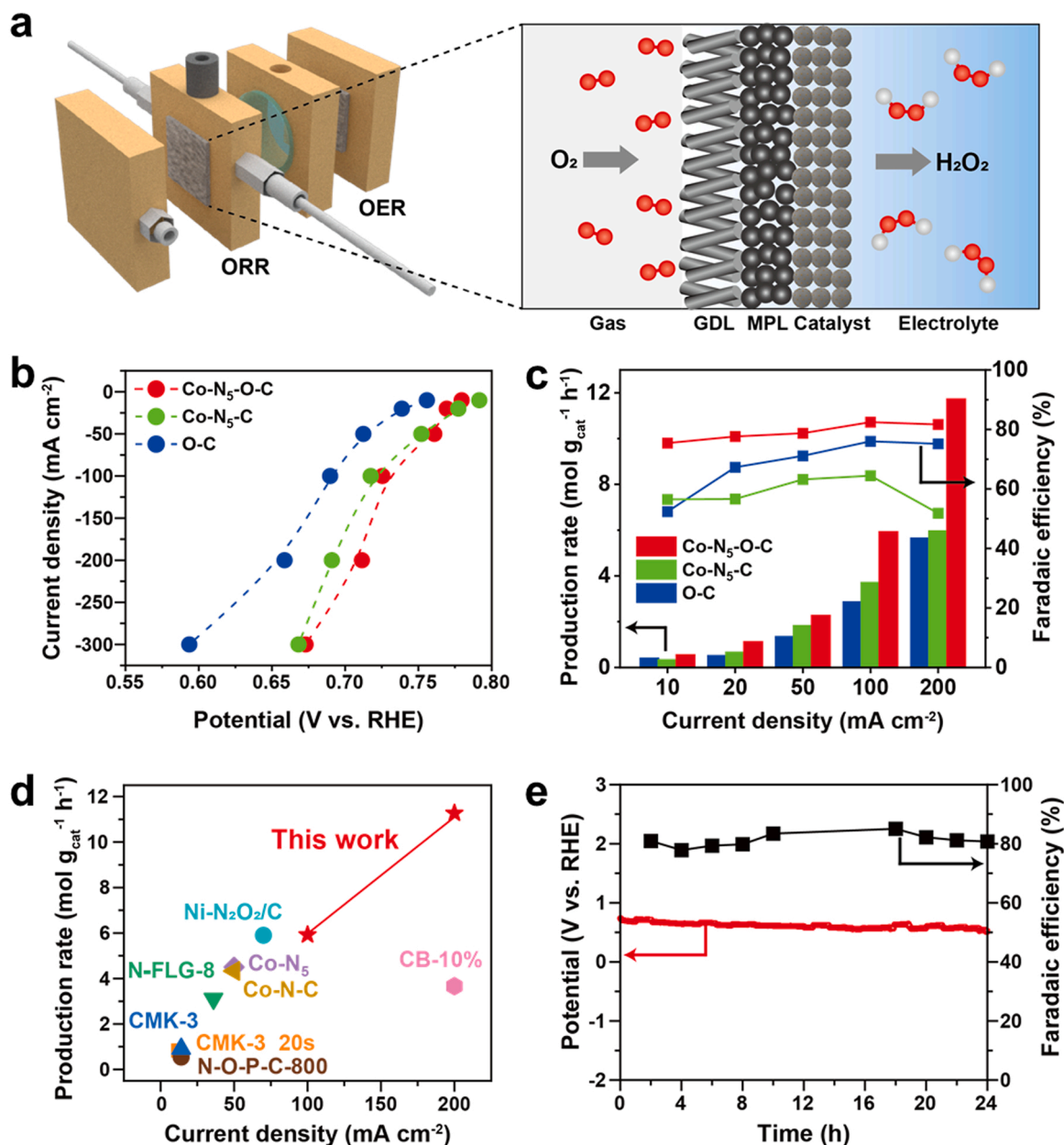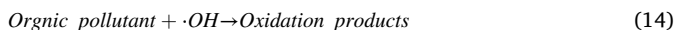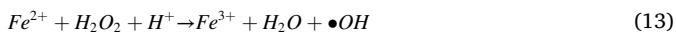
Fig. 5. Three-electrode flow cell performance of the catalysts. a) Schematic illustration of the three-phase flow cell configuration for H_2O_2 mass production. b) I–V curve for O-C, Co-N_5-C, and Co-N_5-O–C in 1 M KOH. c) Faradaic efficiency and H_2O_2 production rate of the catalyst measured under different current densities in 1 M KOH. d) Comparison of the H_2O_2 production rate of Co-N_5-O-C with other reported catalysts. e) Stability test of the Co-N_5-O-C catalyst under 100 mA cm^{-2} in 1 M KOH for 24 h. The electrolyte feeding rate was fixed at 40 mL h^{-1}, and the oxygen feeding rate was fixed at 20 sccm.

Notably, to ensure effective electro-Fenton removal, an effective cathode material for H_2O_2 generation should be chosen.

$$O_2 + 2H^+ + 2e^- \rightarrow H_2O_2 \qquad (12)$$

$$Fe^{2+} + H_2O_2 + H^+ \rightarrow Fe^{3+} + H_2O + \bullet OH \qquad (13)$$

$$Orgnic\ pollutant + \cdot OH \rightarrow Oxidation\ products \qquad (14)$$

$$Fe^{3+} + e^- \rightarrow Fe^{2+} \qquad (15)$$

Here, we used a toxic, carcinogenic, and non-biodegradable pollutant methylene blue (MB) to demonstrate the catalytic effect of the Co-N_5-O-C sample on the electro-Fenton process (Fig. 6a) [58]. Electro-Fenton degradation tests were performed at room temperature in an O_2-saturated 0.05 M Na_2SO_4 solution in the presence of both MB

(20 mg/L) and Fe^{2+} (0.05 mM) in an undivided setup operated at a constant potential (3 V), which used a Co-N_5-O-C catalyst loading (0.4 mg cm^{-2}) on conductive carbon fiber paper (CFP) as the working cathode for efficient H_2O_2 production and a graphite plate for the anode, for which the testing condition was pre-optimized by experiments (Fig. S38 and Note S2). Fig. 6b shows the efficiency comparison of Co/CFP and bare CFP for MB by the electro-Fenton system under the optimum condition. As a result, a similar 20% pre-degradation of MB by physical absorption was visible in both CFP and Co-N_5-O-C/CFP. It is seen that bare CFP can degrade MB gradually with a kinetic rate constant (k = 0.090 min^{-1}), which shows the decay kinetics of most MB in the undivided cell at 4 min by fitting with the theoretical equation of a pseudo-first-order reaction (Fig. S39) [59]. This degradation behavior is probably involved in direct water oxidation of organics at the surface of the anode (M) as in the following Eq. (16),
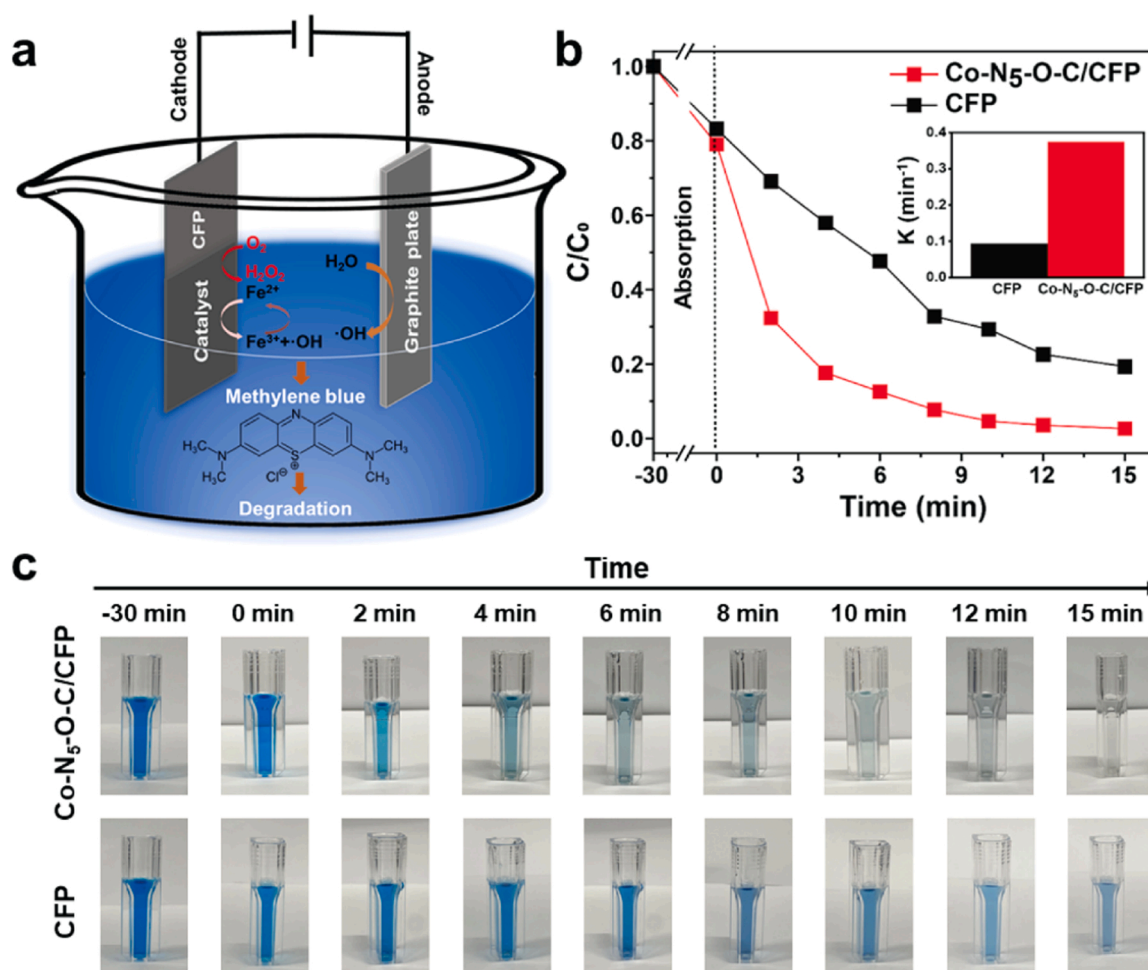
Fig. 6. Electro-Fenton performance of the catalysts. a) Schematic illustration of the electro-Fenton process for Methylene Blue (MB) degradation in an undivided electrolytic cell. b) MB removal efficiency of the catalyst-free carbon fiber paper (CFP) and Co-N$_5$-O-C/CFP catalyst (the inset Figure shows each pseudo-first-order rate constant for the Fenton reactions at 4 min). c) Color decays of the electrolyte solutions overtime during the electro-Fenton degradation test.

$$M + H_2O \rightarrow M(\bullet OH) + H^+ + e^- \qquad (16)$$

Moreover, the use of a graphite plate anode could promote the conversion of M(·OH) into a chemisorbed MO species, leading to the oxidation of the organics mainly into carboxylic acids and boosting the Fenton reaction [60]. Therefore, both the anode oxidation and H$_2$O$_2$-oriented ORR behavior of the cathode are attributed to the absence of impurity in pollutants [61]. While remarkably, when loading Co-N$_5$-O-C on CFP, the MB degradation of the system could be boosted obviously because its kinetic rate constant (k = 0.375 min^{-1}) is nearly 4.2-times higher than that of CFP. Specifically, Co-N$_5$-O-/CFP achieved 100% MB removal within 8 min whereas only 80% was degraded by CFP after a 15 min reaction, which is consistent with the prominent difference in color decay over time shown in Fig. 6c. Thus, these results show that Co-N$_5$-O-C can be a very promising cathode material for the electro-Fenton process and wastewater treat treatment applications.

4. Conclusions

To summarize, we demonstrate a highly coordinated and epoxy-rich Co-N$_5$-O-C catalyst for the 2e$^-$ ORR for the first time. By introducing epoxy functional groups around the highly coordinated Co-N$_5$ moieties to form Co-N$_5$-O-C SACs, both the activity and selectivity towards H$_2$O$_2$ production can be significantly improved compared to the catalysts containing only the Co-N$_5$ moiety without epoxy groups. Remarkably, the electrochemical testing results of the Co-N$_5$-O-C SACs show that a selectivity of up to 85.6% can be readily reached at 0.75 V vs. RHE with an excellent mass activity of 87.5 A g^{-1}. A flow cell test also revealed that the Co-N$_5$-O-C SACs can achieve a high H$_2$O$_2$ production rate of 11.3 mol g^{-1} h^{-1} at a current density of 200 mA cm^{-2} with superior stability and a selectivity of ~80% which was maintained for 24 h of testing. The DFT calculations confirmed that the overpotential of Co-N$_5$ for the 2e$^-$ ORR process can be lower with the introduction of epoxy groups nearby the metal active sites, particularly, with the two epoxy oxygen atoms adjacent to the Co-N$_5$ center, in which the reaction intermediates have the near-ideal binding energy and higher selectivity toward H$_2$O$_2$ production. The electron-withdraw character of the epoxy groups located near the Co-N$_5$ centers helps weaken the binding energy of the absorbed intermediates on the Co-active sites, leading to enhanced activity of H$_2$O$_2$ electrosynthesis. This work highlights the importance of synthetic parameters and procedures in affecting the atomistic structure and composition of SACs. It could motivate studies on establishing synthesis-structure-performance correlations toward the rational design of SACs. Moreover, effective in-situ H$_2$O$_2$ generation was also proven by the rapid degradation of the chosen recalcitrant pollutant in wastewater, showing its promising applications for on-site water treatment.

CRediT authorship contribution statement

Wenjun Zhang: Conceptualization, Methodology, Investigation, Writing – original draft. **Jae Won Choi:** Conceptualization, Formal

analysis, Investigation, Writing – original draft. **Sooyeon Kim:** Conceptualization, Data curation, Investigation, Writing – original draft. **Thao Thi Le:** Methodology, Investigation. **Subhajit Nandy:** Methodology, Investigation. **Chang-Kyu Hwang:** Formal analysis, Validation. **Sae Yane Paek:** Formal analysis, Validation. **Ayeong Byeon:** Data curation, Visualization. **Keun Hwa Chae:** Methodology, Investigation. **Seung Yong Lee:** Data curation, Resources. **Sang Hoon Kim:** Data curation, Resources. **Hakhyeon Song:** Formal analysis, Validation. **Jaehoon Kim:** Formal analysis, Validation. **Jihun Oh:** Methodology, Resources. **Jae W. Lee:** Methodology, Resources. **Sang Soo Han:** Supervision, Project administration, Funding acquisition, Writing – review & editing. **Jong Min Kim:** Supervision, Project administration, Funding acquisition, Conceptualization, Writing - review & editing.

Declaration of Competing Interest

The authors declare that they have no known competing financial interests or personal relationships that could have appeared to influence the work reported in this paper.

Data Availability

No data was used for the research described in the article.

Acknowledgements

Appendix A. Supporting information

Supplementary data associated with this article can be found in the online version at doi:10.1016/j.apcatb.2023.122712.

References

[1] R. Ciriminna, L. Albanese, F. Meneguzzo, M. Pagliaro, Hydrogen peroxide: a key chemical for today's sustainable development, ChemSusChem 9 (2016) 3374–3381, https://doi.org/10.1002/cssc.201600895.

[2] R.L. Myers, The 100 Most Important Chemical Compounds: A Reference Guide, ABC-CLIO, Santa Barbara, California, USA, 2007.

[3] R. Schick, I. Strasser, H.-H. Stabel, Fluorometric determination of low concentrations of H_2O_2 in water: comparison with two other methods and application to environmental samples and drinking-water treatment, Water Res 31 (1997) 1371–1378, https://doi.org/10.1016/S0043-1354(96)00410-1.

[4] J.M. Campos-Martin, G. Blanco-Brieva, J.L.G. Fierro, Hydrogen peroxide synthesis: an outlook beyond the anthraquinone process, Angew. Chem. Int. Ed. 45 (2006) 6962–6984, https://doi.org/10.1002/anie.200503779.

[5] T. Moreno, J. García-Serna, M.J. Cocero, Direct synthesis of hydrogen peroxide in methanol and water using $scCO_2$ and N_2 as diluents, Green. Chem. 12 (2010) 282–289, https://doi.org/10.1039/B916788A.

[6] D. Kim, H. Nam, Y.-H. Cho, B.C. Yeo, S.-H. Cho, J.-P. Ahn, K.-Y. Lee, S.Y. Lee, S. Han, Unlocking the potential of nanoparticles composed of immiscible elements for direct H_2O_2 synthesis, ACS Catal. 9 (2019) 8702–8711, https://doi.org/10.1021/acscatal.9b00451.

[7] Y. Jiang, P. Ni, C. Chen, Y. Lu, P. Yang, B. Kong, A. Fisher, X. Wang, Selective electrochemical H_2O_2 production through two-electron oxygen electrochemistry, Adv. Energy Mater. 8 (2018), 1801909, https://doi.org/10.1002/aenm.201801909.

[8] J. Xu, X. Zheng, Z. Feng, Z. Lu, Z. Zhang, W. Huang, Y. Li, D. Vuckovic, Y. Li, S. Dai, G. Chen, K. Wang, H. Wang, J.K. Chen, W. Mitch, Y. Cui, Organic wastewater treatment by a single-atom catalyst and electrolytically produced H_2O_2, Nat. Sustain. 4 (2021) 233–241, https://doi.org/10.1038/s41893-020-00635-w.

[9] C. Xia, Y. Xia, P. Zhu, L. Fan, H. Wang, Direct electrosynthesis of pure aqueous H_2O_2 solutions up to 20% by weight using a solid electrolyte, Science 366 (2019) 226–231, https://doi.org/10.1126/science.aay1844.

[10] Z. Chen, S. Chen, S. Siahrostami, P. Chakthranont, C. Hahn, D. Nordlund, S. Dimosthenis, J.K. Nørskov, Z. Bao, T.F. Jaramillo, Development of a reactor with carbon catalysts for modular-scale, low-cost electrochemical generation of H_2O_2, React. Chem. Eng. 2 (2017) 239–245, https://doi.org/10.1039/C6RE00195E.

[11] X. Zhang, Y. Xia, C. Xia, H. Wang, Insights into practical-scale electrochemical H2O2 synthesis, Trends Chem. 2 (2020) 942–953, https://doi.org/10.1016/j.trechm.2020.07.007.

[12] Q. He, T. Xu, J. Li, J. Wang, C. Jin, Q. Chen, X. Gu, X. Wang, J. Wei, H. Duan, Y. Gong, Confined PdMo ultrafine nanowires in CNTs for superior oxygen reduction catalysis, Adv. Energy Mater. 12 (2022), 2200849, https://doi.org/10.1002/aenm.202200849.

[13] W. Liu, C. Zhang, J. Zhang, X. Huang, M. Song, J. Li, F. He, H. Yang, J. Zhang, D. Wang, Tuning the atomic configuration of Co-N-C electrocatalyst enables highly-selective H_2O_2 production in acidic media, Appl. Catal. B: Environ. 310 (2022) 121312, https://doi.org/10.1016/j.apcatb.2022.121312.

[14] Y. Sun, L. Silvioli, N.R. Sahraie, W. Ju, J. Li, A. Zitolo, S. Li, A. Bagger, L. Arnarson, X. Wang, T. Moeller, D. Bernsmeier, J. Rossmeisl, F. Jaouen, P. Strasser, Activity–selectivity trends in the electrochemical production of hydrogen peroxide over single-site metal–nitrogen–carbon catalysts, J. Am. Chem. Soc. 141 (2019) 12372–12381, https://doi.org/10.1021/jacs.9b05576.

[15] J. Gao, H. bin Yang, X. Huang, S.-F. Hung, W. Cai, C. Jia, S. Miao, H.M. Chen, X. Yang, Y. Huang, T. Zhang, B. Liu, Enabling direct H_2O_2 production in acidic media through rational design of transition metal single atom catalyst, Chem 6 (2020) 658–674, https://doi.org/10.1016/j.chempr.2019.12.008.

[16] Q. Yang, W. Xu, S. Gong, G. Zheng, Z. Tian, Y. Wen, L. Peng, L. Zhang, Z. Lu, L. Chen, Atomically dispersed Lewis acid sites boost 2-electron oxygen reduction activity of carbon-based catalysts, Nat. Commun. 11 (2020) 5478, https://doi.org/10.1038/s41467-020-19309-4.

[17] F. Wu, C. Pan, C.-T. He, Y. Han, W. Ma, H. Wei, W. Ji, W. Chen, J. Mao, P. Yu, D. Wang, L. Mao, Y. Li, Single-atom Co–N_4 electrocatalyst enabling four-electron oxygen reduction with enhanced hydrogen peroxide tolerance for selective sensing, J. Am. Chem. Soc. 142 (2020) 16861–16867, https://doi.org/10.1021/jacs.0c07790.

[18] C. Tang, L. Chen, H. Li, L. Li, Y. Jiao, Y. Zheng, H. Xu, K. Davey, S.-Z. Qiao, Tailoring acidic oxygen reduction selectivity on single-atom catalysts via modification of first and second coordination spheres, J. Am. Chem. Soc. 143 (2021) 7819–7827, https://doi.org/10.1021/jacs.1c03135.

[19] W. Li, F. Li, H. Yang, X. Wu, P. Zhang, Y. Shan, L. Sun, A bio-inspired coordination polymer as outstanding water oxidation catalyst via second coordination sphere engineering, Nat. Commun. 10 (2019) 5074, https://doi.org/10.1038/s41467-019-13052-1.

[20] J. Liu, Z. Wei, Z. Gong, M. Yan, Y. Hu, S. Zhao, G. Ye, H. Fei, Single-atom CoN_4 sites with elongated bonding induced by phosphorus doping for efficient H_2O_2 electrosynthesis, Appl. Catal. B: Environ. 324 (2023), 122267, https://doi.org/10.1016/j.apcatb.2022.122267.

[21] J. Liu, Z. Gong, M. Yan, G. He, H. Gong, G. Ye, H. Fei, Electronic structure regulation of single-atom catalysts for electrochemical oxygen reduction to H_2O_2, Small 18 (2022), 2103824, https://doi.org/10.1002/smll.202103824.

[22] E. Zhang, L. Tao, J. An, J. Zhang, L. Meng, X. Zheng, Y. Wang, N. Li, S. Du, J. Zhang, D. Wang, Y. Li, Engineering the local atomic environments of indium single-atom catalysts for efficient electrochemical production of hydrogen peroxide, Angew. Chem. Int. Ed. 61 (2022), e202117347, https://doi.org/10.1002/anie.202117347.

[23] H. Gong, Z. Wei, Z. Gong, J. Liu, G. Ye, M. Yan, J. Dong, C. Allen, J. Liu, K. Huang, R. Liu, G. He, S. Zhao, H. Fei, Low-coordinated Co-N-C on oxygenated graphene for efficient electrocatalytic H_2O_2 production, Adv. Funct. Mater. 32 (2022), 2106886, https://doi.org/10.1002/adfm.202106886.

[24] Q. Zhao, Y. Wang, W.-H. Lai, F. Xiao, Y. Lyu, C. Liao, M. Shao, Approaching a high-rate and sustainable production of hydrogen peroxide: oxygen reduction on Co–N–C single-atom electrocatalysts in simulated seawater, Energy Environ. Sci. 14 (2021) 5444–5456, https://doi.org/10.1039/D1EE00878A.

[25] Y. Zhang, J. Liu, J. Wang, Y. Zhao, D. Luo, A. Yu, X. Wang, Z. Chen, Engineering oversaturated Fe-N_5 multifunctional catalytic sites for durable lithium-sulfur, Batter., Angew. Chem. Int. Ed. 60 (2021) 26622–26629, https://doi.org/10.1002/anie.202108882.

[26] S. Zhang, X. Ao, J. Huang, B. Wei, Y. Zhai, D. Zhai, W. Deng, C. Su, D. Wang, Y. Li, Isolated single-atom Ni–N_5 catalytic site in hollow porous carbon capsules for efficient lithium–sulfur batteries, Nano Lett. 21 (2021) 9691–9698, https://doi.org/10.1021/acs.nanolett.1c03499.

[27] H. Zhang, S. Jia, X. Shi, Z. Li, B. Liu, N. Li, Y. Li, S. Hu, H. Wang, Atomic Fe–N5 catalytic sites embedded in N-doped carbon as a highly efficient oxygen electrocatalyst for zinc–air batteries, Mater. Chem. Front. 5 (2021) 8127–8137, https://doi.org/10.1039/D1QM00809A.

[28] Z. Lu, G. Chen, S. Siahrostami, Z. Chen, K. Liu, J. Xie, L. Liao, T. Wu, D. Lin, Y. Liu, T.F. Jaramillo, J.K. Nørskov, Y. Cui, High-efficiency oxygen reduction to hydrogen peroxide catalysed by oxidized carbon materials, Nat. Catal. 1 (2018) 156–162, https://doi.org/10.1038/s41929-017-0017-x.

[29] H.W. Kim, M.B. Ross, N. Kornienko, L. Zhang, J. Guo, P. Yang, B.D. McCloskey, Efficient hydrogen peroxide generation using reduced graphene oxide-based oxygen reduction electrocatalysts, Nat. Catal. 1 (2018) 282–290, https://doi.org/10.1038/s41929-018-0044-2.

[30] J.S. Lim, J.H. Kim, J. Woo, D.S. Baek, K. Ihm, T.J. Shin, Y.J. Sa, S.H. Joo, Designing highly active nanoporous carbon H_2O_2 production electrocatalysts through active site identification, Chem 7 (2021) 3114–3130, https://doi.org/10.1016/j.chempr.2021.08.007.

[31] Q. Zhang, X. Tan, N.M. Bedford, Z. Han, L. Thomsen, S. Smith, R. Amal, X. Lu, Direct insights into the role of epoxy groups on cobalt sites for acidic H_2O_2 production, Nat. Commun. 11 (2020) 4181, https://doi.org/10.1038/s41467-020-17782-5.

[32] W. Liu, J. Feng, R. Yin, Y. Ni, D. Zheng, W. Que, X. Niu, X. Dai, W. Shi, F. Wu, J. Yang, X. Cao, Tailoring oxygenated groups of monolithic cobalt-nitrogen-carbon frameworks for highly efficient hydrogen peroxide production in acidic media, Chem. Eng. J. 430 (2022), 132990, https://doi.org/10.1016/j.cej.2021.132990.

[33] H. Yang, L. Shang, Q. Zhang, R. Shi, G.I.N. Waterhouse, L. Gu, T. Zhang, A universal ligand mediated method for large scale synthesis of transition metal single atom catalysts, Nat. Commun. 10 (2019) 4585, https://doi.org/10.1038/s41467-019-12510-0.

[34] H. Sheng, E.D. Hermes, X. Yang, D. Ying, A.N. Janes, W. Li, J.R. Schmidt, S. Jin, Electrocatalytic production of H₂O₂ by selective oxygen reduction using earth-abundant cobalt pyrite (CoS₂), ACS Catal. 9 (2019) 8433–8442, https://doi.org/10.1021/acscatal.9b02546.

[35] G. Kresse, J. Hafner, *Ab initio* molecular-dynamics simulation of the liquid-metal–amorphous-semiconductor transition in germanium, Phys. Rev. B 49 (1994) 14251–14269, https://doi.org/10.1103/PhysRevB.49.14251.

[36] G. Kresse, J. Furthmüller, Efficient iterative schemes for ab initio total-energy calculations using a plane-wave basis set, Phys. Rev. B. 54 (1996) 11169, https://doi.org/10.1103/PhysRevB.54.11169.

[37] P.E. Blöchl, Projector augmented-wave method, Phys. Rev. B. 50 (1994) 17953–17979, https://doi.org/10.1103/PhysRevB.50.17953.

[38] J.P. Perdew, K. Burke, M. Ernzerhof, Generalized gradient approximation made simple, Phys. Rev. Lett. 77 (1996) 3865–3868, https://doi.org/10.1103/PhysRevLett.77.3865.

[39] S. Grimme, J. Antony, S. Ehrlich, H. Krieg, A consistent and accurate ab initio parametrization of density functional dispersion correction (DFT-D) for the 94 elements H-Pu, J. Chem. Phys. 132 (2010), 154104, https://doi.org/10.1063/1.3382344.

[40] K. Mathew, R. Sundararaman, K. Letchworth-Weaver, T.A. Arias, R.G. Hennig, Implicit solvation model for density-functional study of nanocrystal surfaces and reaction pathways, J. Chem. Phys. 140 (2014), 084106, https://doi.org/10.1063/1.4865107.

[41] J.K. Nørskov, J. Rossmeisl, A. Logadottir, L. Lindqvist, J.R. Kitchin, T. Bligaard, H. Jónsson, Origin of the overpotential for oxygen reduction at a fuel-cell cathode, J. Phys. Chem. B 108 (2004) 17886–17892, https://doi.org/10.1021/jp047349j.

[42] G. Henkelman, B.P. Uberuaga, H. Jónsson, A climbing image nudged elastic band method for finding saddle points and minimum energy paths, J. Chem. Phys. 113 (2000) 9901–9904, https://doi.org/10.1063/1.1329672.

[43] T.M. Do, J.Y. Byun, S.H. Kim, An electro-Fenton system using magnetite coated metallic foams as cathode for dye degradation, Catal. Today 295 (2017) 48–55, https://doi.org/10.1016/j.cattod.2017.05.016.

[44] Y.J. Choe, J. Kim, J.Y. Byun, S.H. Kim, An electro-Fenton system with magnetite coated stainless steel mesh as cathode, Catal. Today 359 (2021) 16–22, https://doi.org/10.1016/j.cattod.2019.06.062.

[45] R.M. Reis, R.B. Valim, R.S. Rocha, A.S. Lima, P.S. Castro, M. Bertotti, M.R.V. Lanza, The use of copper and cobalt phthalocyanines as electrocatalysts for the oxygen reduction reaction in acid medium, Electrochim. Acta 139 (2014) 1–6, https://doi.org/10.1016/j.electacta.2014.07.003.

[46] W.R.P. Barros, R.M. Reis, R.S. Rocha, M.R.V. Lanza, Electrogeneration of hydrogen peroxide in acidic medium using gas diffusion electrodes modified with cobalt (II) phthalocyanine, Electrochim. Acta (2013) 12–18, https://doi.org/10.1016/j.electacta.2013.04.079.

[47] W. Liu, Y. Chen, H. Qi, L. Zhang, W. Yan, X. Liu, X. Yang, S. Miao, W. Wang, C. Liu, A. Wang, J. Li, T. Zhang, A durable nickel single-atom catalyst for hydrogenation

reactions and cellulose valorization under harsh conditions, Angew. Chem., Int. Ed. 57 (2018) 7071–7075, https://doi.org/10.1002/anie.201802231.

[48] E. Jung, H. Shin, B.-H. Lee, V. Efremov, S. Lee, H.S. Lee, J. Kim, W. Hooch Antink, S. Park, K.-S. Lee, S.-P. Cho, J.S. Yoo, Y.-E. Sung, T. Hyeon, Atomic-level tuning of Co–N–C catalyst for high-performance electrochemical H₂O₂ production, Nat. Mater. 19 (2020) 436–442, https://doi.org/10.1038/s41563-019-0571-5.

[49] S. Dursun, M.S. Yazici, Mixed carbon-graphene supports for cobalt (II) phthalocyanine as fuel cell cathode, ECS J. Solid State Sci. Technol. 9 (2020), 041008, https://doi.org/10.1149/2162-8777/ab8787.

[50] K. Müller, M. Richter, D. Friedrich, I. Paloumpa, U.I. Kramm, D. Schmeißer, Spectroscopic characterization of cobalt–phthalocyanine electrocatalysts for fuel cell applications, Solid State Ion. 216 (2012) 78–82, https://doi.org/10.1016/j.ssi.2011.12.013.

[51] S. Siahrostami, A. Verdaguer-Casadevall, M. Karamad, D. Deiana, P. Malacrida, B. Wickman, M. Escudero-Escribano, E.A. Paoli, R. Frydendal, T.W. Hansen, I. Chorkendorff, I.E.L. Stephens, J. Rossmeisl, Enabling direct H2O2 production through rational electrocatalyst design, Nat. Mater. 12 (2013) 1137–1143, https://doi.org/10.1038/nmat3795.

[52] S. Siahrostami, S.J. Villegas, A.H. Bagherzadeh Mostaghimi, S. Back, A.B. Farimani, H. Wang, K.A. Persson, J. Montoya, A review on challenges and successes in atomic-scale design of catalysts for electrochemical synthesis of hydrogen peroxide, ACS Catal. 10 (2020) 7495–7511, https://doi.org/10.1021/acscatal.0c01641.

[53] N. Wang, S. Ma, P. Zuo, J. Duan, B. Hou, Recent progress of electrochemical production of hydrogen peroxide by two-electron oxygen reduction reaction, Adv. Sci. 8 (2021), 2100076, https://doi.org/10.1002/advs.202100076.

[54] Y. Mun, S. Lee, K. Kim, S. Kim, S. Lee, J.W. Han, J. Lee, Versatile strategy for tuning ORR activity of a single Fe-N₄ site by controlling electron-withdrawing/donating properties of a carbon plane, J. Am. Chem. Soc. 141 (2019) 6254–6262, https://doi.org/10.1021/jacs.8b13543.

[55] J. Park, H. Oh, T. Ha, Y.I. Lee, K. Min, A review of the gas diffusion layer in proton exchange membrane fuel cells: durability and degradation, Appl. Energy 155 (2015) 866–880, https://doi.org/10.1016/j.apenergy.2015.06.068.

[56] X. Teng, J. Li, Z. Wang, Z. Wei, C. Chen, K. Du, C. Zhao, G. Yang, Y. Li, Performance and mechanism of methylene blue degradation by an electrochemical process, RSC Adv. 10 (2020) 24712–24720, https://doi.org/10.1039/D0RA03963B.

[57] H. Sheng, A.N. Janes, R.D. Ross, D. Kaiman, J. Huang, B. Song, J.R. Schmidt, S. Jin, Stable and selective electrosynthesis of hydrogen peroxide and the electro-Fenton process on CoSe₂ polymorph catalysts, Energy Environ. Sci. 13 (2020) 4189–4203, https://doi.org/10.1039/D0EE01925A.

[58] M. Panizza, A. Barbucci, R. Ricotti, G. Cerisola, Electrochemical degradation of methylene blue, Sep. Purif. Technol. 54 (2007) 382–387, https://doi.org/10.1016/j.seppur.2006.10.010.

[59] E. Brillas, I. Sirés, M.A. Oturan, Electro-Fenton process and related electrochemical technologies based on Fenton's reaction chemistry, Chem. Rev. 109 (2009) 6570–6631, https://doi.org/10.1021/cr900136g.

[60] F. Sopaj, N. Oturan, J. Pinson, F. Podvorica, M.A. Oturan, Effect of the anode materials on the efficiency of the electro-Fenton process for the mineralization of the antibiotic sulfamethazine, Appl. Catal. B: Environ. 199 (2016) 331–341, https://doi.org/10.1016/j.apcatb.2016.06.035.

[61] J. Wang, S. Li, Q. Qin, C. Peng, Sustainable and feasible reagent-free electro-Fenton via sequential dual-cathode electrocatalysis, Proc. Natl. Acad. Sci. U. S. A. 118 (2021), e2108573118, https://doi.org/10.1073/pnas.2108573118.